PCCP

PAPER

View Article Online
View Journal | View Issue

Published on 02 September 2021. Downloaded by TU Berlin - Universitaetsbibl on 2/22/2022 10:28:25 AM.

Check for updates

Cite this: *Phys. Chem. Chem. Phys.*, 2021, **23**, 20129

Exceptionally high saturation magnetisation in Eu-doped magnetite stabilised by spin–orbit interaction†

M. Hussein N. Assadi, *[a] José Julio Gutiérrez Moreno,[b] Dorian A. H. Hanaor[c] and Hiroshi Katayama-Yoshida[d]

Received 17th May 2021,
Accepted 10th August 2021

DOI: 10.1039/d1cp02164h

rsc.li/pccp

The significance of the spin–orbit interaction is very well known in compounds containing heavier elements such as the rare-earth Eu ion. Here, through density functional calculations, we investigated the effect of the spin–orbit interaction on the magnetic ground state of Eu doped magnetite (Fe_3O_4:Eu_{Fe}). By examining all possible spin alignments between Eu and magnetite's Fe, we demonstrate that Eu, which is most stable when doped at the tetrahedral site, adapts a spin almost opposite the substituted Fe. Consequently, because of smaller spin cancellation between the cations on the tetrahedral site (Fe_{Tet} and Eu_{Tet}) and the cations on the octahedral sites (Fe_{Oct}), Fe_3O_4:Eu_{Fe} exhibits a maximum saturation magnetisation of 9.451 μ_B per f.u. which is significantly larger than that of undoped magnetite (calculated to be 3.929 μ_B per f.u.). We further show that this large magnetisation persists through additional electron doping. However, additional hole doping, which may unintentionally occur in Fe deficient magnetite, can reduce the magnetisation to values smaller than that of the undoped magnetite. The results presented here can aid in designing highly efficient magnetically recoverable catalysts for which both magnetite and rare earth dopants are common materials.

Introduction

Magnetite (Fe_3O_4) has been the most widely used permanent magnet since around the 9th century BCE, with its discovery and the origin of the word magnet being attributed to Magnes the shepherd.[1] In more recent times, magnetite thin films and nanoparticles, particularly in doped forms, have found a wide range of applications in environmental remediation,[2] spintronics,[3,4] catalysis,[5] drug delivery,[6] and biomedical applications.[7] At room temperature, magnetite has a face-centred cubic (fcc) structure (Fig. 1). In this structure, one-third of Fe ions occupy tetrahedral sites (Fe_{Tet}) with a 3+ oxidation state, while the remaining two-thirds occupy the octahedral site (Fe_{Oct}) and are equally likely to be in either 2+ or 3+ oxidation state. This cationic distribution is commonly referred to as an inverse spinel. In a spinel structure, in contrast, all cations at the tetrahedral sites are in the 2+ oxidation state, while all cations in the octahedral sites are in the 3+ oxidation state. Despite having a significant net magnetic moment measured at ~4.1 μ_B and magnetic saturation of ~93 emu g^{-1} at room temperature,[8] magnetite is in fact a ferrimagnet, meaning that the spin of the tetrahedral Fe ions opposes the spin of the octahedral Fe ions.[9,10] Nonetheless, even with the spin

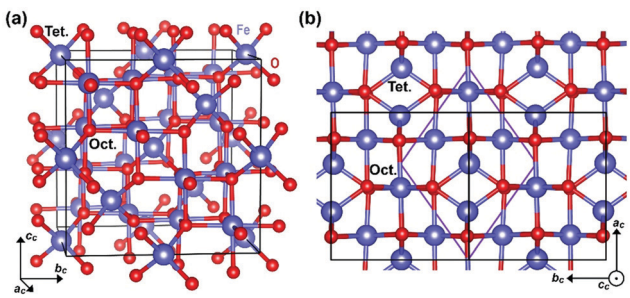

Fig. 1 (a) Conventional cell of inverse spinel form Fe_3O_4, which is face-centred-cubic, *i.e.*, $Fd\bar{3}m$ (227) space group and containing 56 atoms. Fe ions on the octahedral site have a spin direction opposite to that of Fe ions on the tetrahedral sites. (b) The primitive cell of Fe_3O_4 containing 14 atoms is marked with purple boundaries. Light blue and red spheres denote Fe and O, respectively.

[a] School of Materials Science and Engineering, The University of New South Wales, NSW 2052, Australia. E-mail: h.assadi.2008@ieee.org
[b] Department of Computer Applications in Science and Engineering, Barcelona Supercomputing Center (BSC), C/Jordi Girona 31, 08034 Barcelona, Spain
[c] Fachgebiet Keramische Werkstoffe, Technische Universität Berlin, 10623 Berlin, Germany
[d] Center for Spintronics Research Network, Graduate School of Engineering, The University of Tokyo, 7-3-1 Hongo, Bunkyo-ku, Tokyo 113-8656, Japan

† Electronic supplementary information (ESI) available. See DOI: 10.1039/d1cp02164h

Published on 02 September 2021. Downloaded by TU Berlin - Universitaetsbibl on 2/22/2022 10:28:25 AM.

cancellations, as Fe ions are in high spin states (Fe^{2+}: S = 2, Fe^{3+}: S = 5/2), the remainder of the magnetic moment is still large.

Often magnetite is doped with other cations to improve its electrical, optical or catalytic functionalities. Among the dopants, rare earth elements (lanthanides) are a popular choice due to their 3+ oxidation state and their unique optical and magnetic properties, which are related to the presence of partially filled f electronic orbitals.[11–28] Given the higher atomic mass and substantially larger atomic radii of the rare earth elements compared to Fe and O, one would wonder what the role of the spin–orbit interaction is in determining the structure and electronic features of the rare earth doped magnetite. Spin–orbit interactions originate from the coupling between an electron's spin and the magnetic field induced by the relative motion of the nucleus with respect to the electron.[29] The strength of the magnetic interaction increases with the mass of the element in a complex manner.[30] Summarily, for valence electrons, the spin–orbit interaction strength scales somewhere between the lower bound of the Landau–Lifshitz scaling at Z^2 (Z is the atomic number) and the higher bound of Z^4 obtained by the hydrogenic approximation.[31] In any case, the spin–orbit interaction becomes significant in determining the magnetic ground state of the 4d, 5d, and 4f compounds.

In the absence of spin–orbit coupling, the orbital moment ($\boldsymbol{l}$) and the spin ($\boldsymbol{s}$) are independent quantum descriptors of a system. Consequently, a compound's magnetic ground state depends only on the relative orientation of the spin of its magnetic ions with respect to each other. Hence, identifying the magnetic ions as having either spin-up or spin-down suffices in describing the magnetic configuration, as rotating all magnetic moments simultaneously by the same angle does not change the energy. However, when spin–orbit interactions become significant, $\boldsymbol{l}$ and $\boldsymbol{s}$ cease to be independent, as the spin–orbit interaction contains the term $\boldsymbol{l}\cdot\boldsymbol{s}$. In such a case, the spin directions of the magnetic moment should be described with respect to the crystallographic directions. Moreover, the spin–orbit interaction often results in magnetic noncollinearity, where the spins on different crystallographic sites may take an arbitrary orientation with respect to one another, instead of being strictly parallel or antiparallel.[32]

Given the argument above, one would anticipate that the spin–orbit interaction's role is significant in rare-earth-doped magnetite systems. However, this interaction is unlikely to play a dominant role in governing the properties of undoped magnetite. Although some previous studies have discussed the structural, optical and magnetic properties of Eu-doped magnetite[12,16] processed by different experimental methods, more fundamental studies aiming at deeper insights into the magnetic properties of Eu-doped magnetite based on the analysis of spin–orbit interactions are still lacking. Here, motivated by closing this gap, we examine the structural, magnetic and electronic properties of Eu as a representative of the lanthanides doped magnetite. We demonstrate that Eu doping introduces significant noncollinearity, which greatly enhances the saturation magnetisation in magnetite. Furthermore, we show that additional hole doping destabilises the magnetic coupling in Eu-doped magnetite.

Methods and models

Noncollinear density functional calculations, which include the spin–orbit interaction, were performed with VASP,[33,34] using the projector augmented wave method (PAW) technique[35] and the Perdew–Burke–Ernzerhof (PBE) exchange–correlation functional,[36] which is based on the general gradient approximation. In VASP, the spin–orbit interaction is added to the electronic part of the PAW Hamiltonian and solved variationally, while PAW pseudopotentials account for the mass velocity and Darwin terms. To improve the band description, adequate intra-atomic interaction terms (U_{eff}), based on the approach proposed by Liechtenstein *et al.*,[37] were added to Fe 3d and Eu 4f states. The U_{eff} was 5.3 eV (U = 5.3 eV and J = 0.0 eV) for Fe 3d electrons and 7.7 eV (U = 8.7 eV and J = 1.0 eV) for Eu 4f electrons. Comparable values were reported to improve the calculation accuracy of rare-earth compounds[38–40] and magnetite.[41,42] Furthermore, as shown in Fig. S1 (ESI†), the applied U_{eff} values were necessary to adequately localise the 4f and 3d electrons. The energy cut-off was set at 520 eV. The precision key for the rest of the parameters was set high. The noncollinear calculations were initiated with the wave functions calculated with the spin-polarised collinear method to aid convergence. The results for collinear and noncollinear calculations are compared in Fig. S2 (ESI†). Accordingly, noncollinear calculations consistently resulted in lower total energies, indicating higher stability.

For the simulation of Eu_{Fe} doping, a tetrahedral Fe in the primitive Fe_3O_4 cell, enclosed in purple boundaries in Fig. 1b, was substituted with Eu. This primitive cell initially contained two tetrahedral Fe and four octahedral Fe. The substitution of Eu in the tetrahedral site was justified by examining all spin configurations of octahedrally Eu-doped magnetite, both with and without carrier codoping. As shown in Fig. S3 (ESI†), we found that Eu substitution at Fe_{Oct} sites had at least $\sim$1 eV higher formation energy than Eu substituting for Fe_{Tet}. In other words, Fig. S3 (ESI†) indicates that under equilibrium synthesis, Eu energetically favours tetrahedral substitution. In this simulation, the replacement of one Fe for Eu results in a cationic doping concentration of 16.67%. For simulating electron and hole doping, one oxygen was substituted with either N (N_O) or F (F_O).[43] N_O simulates hole doping, while F_O simulates electron doping at 12.5% carrier doping with respect to the total concentration of O. Adding anionic co-dopants for simulating carrier codoping is a common method to avoid simulations of charged supercell which introduce artificial dipole–dipole interactions.[44,45] As articulated in Fig. S4 (ESI†), N/F codopants were placed at the most stable sites within the lattice.

For geometry optimisation, the internal coordinates and the lattice parameters were allowed to relax to energies and forces smaller than 10^{-6} eV and 0.01 eV Å^{-1}, respectively. A dense k-point mesh, generated with the Monkhorst–Pack scheme of

 This journal is © the Owner Societies 2021

Published on 02 September 2021. Downloaded by TU Berlin - Universitaetsbibl on 2/22/2022 10:28:25 AM.

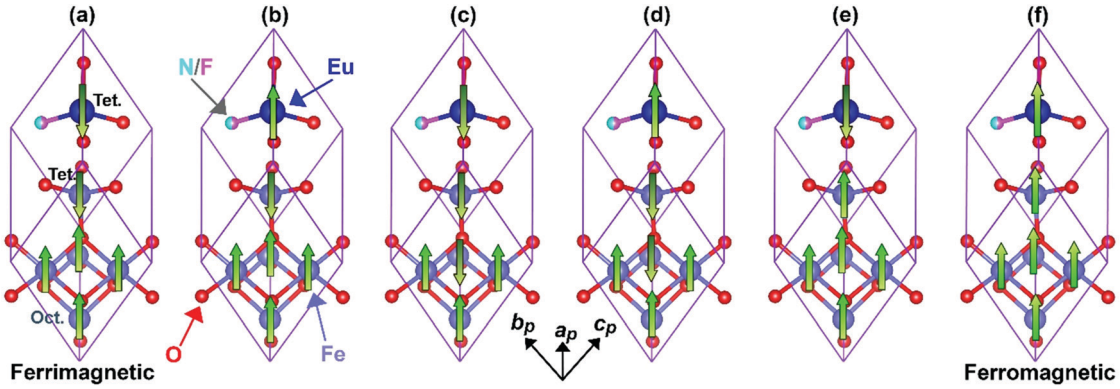

Fig. 2 The initial spin alignments investigated for finding the ground state of Eu-doped and carrier codoped Fe_3O_4. Hole or electron doping was simulated by replacing an oxygen ion with a nitrogen or fluorine ion.

$\sim$0.05 $Å^{-1}$ spacing, consisting of 256 irreducible sampling points in the Brillouin zone, was used for geometry optimisation, ensuring accurately calculated forces for obtaining relaxed structures. This level of accuracy was required as final geometries are sensitive to the magnetic configuration.[46] The density of states (DOS) was calculated with a denser mesh of 343 irreducible *k*-points to adequately capture sharply localised states, along with the tetrahedron smearing method with Blöch corrections at a σ of 0.05.

Six initial spin configurations, shown in Fig. 2 and labelled (a) through (f), were examined to compare the relative stability of different possible magnetic alignments among Fe ions and the Eu dopant. In configuration (a), Eu_{Fe} and Fe_{Tet} were set to have opposite spins to the Fe_{Oct} ions, similar to the ferrimagnetic configuration of pristine Fe_3O_4. In configuration (b), the spin direction of Eu_{Fe} was set opposite to that of Fe_{Tet} and parallel to the spin of the Fe_{Oct} ions. Configurations (a) and (b) were chosen to examine whether or not Eu_{Tet} adopts a spin direction similar to the replaced Fe_{Tet} ion. The spin direction of Fe_{Tet} and Eu_{Fe} in configurations (c) and (d) are similar to those in (a) and (b), except that the spin direction of a Fe_{Oct} ion adjacent to Eu_{Fe} was flipped to examine whether Eu_{Fe} affects the spin direction of any octahedral Fe. In configuration (e), the spin direction of Eu_{Fe} conforms to that of the Fe_{Tet} it replaces, while the spin direction of the remaining Fe_{Tet} was flipped. This configuration served to examine if Eu_{Tet} would affect the spin direction of the remaining tetrahedral Fe. In configuration (f), all cations' spin direction was set parallel to examine the possibility of Eu_{Te} inducing ferromagnetic spin alignment in magnetite.

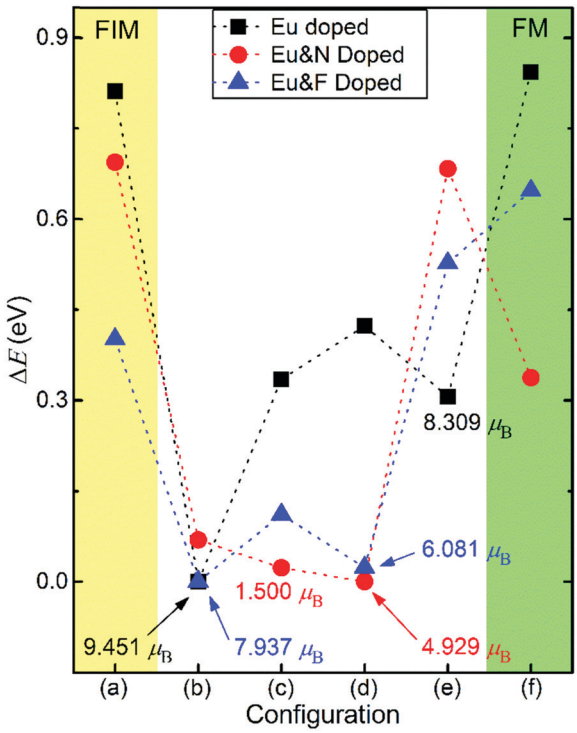

Fig. 3 The relative energy of the optimised configurations presented in Fig. 2. FIM and FM stand for ferrimagnetic and ferromagnetic, respectively. The net magnetisation of the two most stable configurations is also provided.

Results and discussions

For the Fe_3O_4:Eu_{Fe} system, as shown in Fig. 3, the optimised structure of configuration (b) was found to be the most stable. As shown in Fig. 4a, the tetrahedral Fe has an almost antiparallel spin to octahedral Fe ions. The Fe_{Tet} spin's angle to the net spin of the Fe_{Oct} ions was practically complete at 179.56°. However, the Eu ion's spin was, to a good approximation, antiparallel to that of Fe_{Tet}, having an obtuse angle of 175.16°. The Eu_{Fe}'s spin alignment was opposite to what the original tetrahedral Fe would have been, which is parallel to the other Fe_{Tet}. As a consequence of the smaller spin cancellation from the tetrahedral sites, the net magnetisation of the Fe_3O_4:Eu_{Fe}, calculated to be 9.451 μ_B per f.u., was significantly larger than that of the pristine Fe_3O_4, which has been measured to be $\sim$4.1 μ_B per f.u.,[8] and calculated to be 3.929 μ_B per f.u. (Table S1, ESI†).

For the hole-doped Fe_3O_4:$Eu_{Fe}N_O$ system, the most stable structure corresponds to the optimised configuration (d). Moreover, as seen in Fig. 4b, the optimisation resulted in a significant spin rotation with respect to the initial spin

Published on 02 September 2021. Downloaded by TU Berlin - Universitaetsbibl on 2/22/2022 10:28:25 AM.

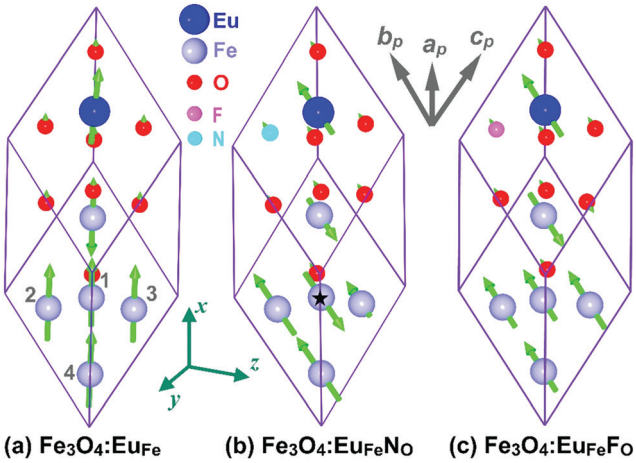

Fig. 4 The most stable spin alignments of the (a) Fe_3O_4:Eu_{Fe}, (b) Fe_3O_4:$Eu_{Fe}N_O$ (p-type doping), and (c) Fe_3O_4:$Eu_{Fe}F_O$ (n-type doping) based on noncollinear calculations. The primitive cell axes are shown at the top, while the orthogonal frame used for projecting the spinors is shown at the bottom. The *x* axis is parallel to the $\boldsymbol{a}_p + \boldsymbol{b}_p + \boldsymbol{c}_p$ vector.

configuration of Fig. 2d. Here, resembling the Fe_3O_4:Eu_{Fe} structure, Eu's spin alignment was almost opposite that of the Fe_{Tet}, taking an obtuse angle of 158.78°. Furthermore, one of the octahedral Fe ions (marked with a star in Fig. 4b) was aligned against the rest of the octahedral Fe ions. The angle between this Fe_{Oct}'s spin and the rest of Fe_{Oct} ions' net spin was 141.38°. The strong noncollinearity and the substantial spin cancellation among Fe_{Oct} ions resulted in a net magnetisation of 4.929 μ_B per f.u. for the Fe_3O_4:$Eu_{Fe}N_O$ system, which is smaller than that of Fe_3O_4:Eu_{Fe}, but still larger than that of undoped Fe_3O_4.

For the electron-doped Fe_3O_4:$Eu_{Fe}F_O$ system, the most stable structure was the optimised configuration (b). Here again, the relaxation resulted in a significant spin rotation with respect to the initial spin alignment. Nonetheless, similar to the last two systems, the Eu ion's spin alignment was against that of the tetrahedral Fe, forming an obtuse angle of 154.44°. The spin directions of the Fe_{Oct} ions were nearly parallel and opposing that of the Fe_{Tet}. The angle between the net spin on Fe_{Oct} ions and that on the Fe_{Tet} ion was almost complete at 179.96°. The net magnetisation for the Fe_3O_4:$Eu_{Fe}F_O$ system was 7.937 μ_B per f.u. which is still more prominent than the undoped Fe_3O_4's magnetisation but smaller than that of the singly Eu-doped system. The reduced magnetisation is mainly because the doped electron reduces one Fe^{3+} (d^5) ion to a Fe^{2+} (d^6) with a smaller spin number.

The net magnetisations calculated above can provide an upper-bound estimation for the saturation magnetisation in real compounds below the paramagnetic transition temperature. Given the nature of the simulation, which is periodic in three dimensions, the calculated net magnetisations result in a similar magnetic saturation in a perfectly ordered, maximally dense, infinitely large and single-domain specimen under a strong external magnetic field. Any deviation of this ideal case lowers the magnetic saturation. The maximum temperatures at which the calculated net magnetisations would be stable can be quantitatively estimated from the stability margin against the second most stable spin configuration. The larger this merging of stability is, the higher thermal fluctuations would be required to destabilise the most stable spin alignment. For example, earlier DFT calculations indicate that in undoped Fe_3O_4, the ferrimagnetic state is more stable than the ferromagnetic state (all Fe ions set with parallel spin alignment) by 0.458 eV per f.u.,[47] resulting in an 858 K Curie temperature.[48]

As shown in Fig. 3, the next most stable spin configuration for the Fe_3O_4:Eu_{Fe} system is the optimised configuration (e), for which the total energy is 0.306 eV per f.u. higher than the most stable configuration (b). This relatively significant energy difference implies room-temperature stability for the optimised configuration (b), although this magnetisation is not as thermally stable as that of undoped Fe_3O_4. For the Fe_3O_4:$Eu_{Fe}N_O$ system, the total energy of the second most stable configuration, optimised configuration (c), is merely 0.023 eV per f.u. higher than the optimised configuration (d), *i.e.*, the most stable configuration. The total magnetisation of configuration (c) is 1.500 μ_B per f.u. Similarly, for the Fe_3O_4:$Eu_{Fe}F_O$ system, the optimised configuration (d) is the second most stable and has a total energy that is 0.024 eV per f.u. higher than that of the most stable configuration (b). In this case, the optimised configuration (d) has a total magnetisation of 6.081 μ_B per f.u. Given the small margin of stability of the magnetic ground state of the hole- and electron-codoped Fe_3O_4:Eu_{Fe}, one does not anticipate their realisation at room temperature as their small margin of stability against competing magnetic configurations may not prevail against thermal fluctuations. Moreover, the competing magnetic phase in hole-doped Fe_3O_4:$Eu_{Fe}N_O$ has substantially smaller net magnetisation at about the third of the most stable configuration. For the electron-doped Fe_3O_4:$Eu_{Fe}O_F$ system, the competing magnetic phase still has a comparable net magnetisation to the most stable configuration.

Eu doped magnetite nanoparticles of ~12 nm size, synthesised with coprecipitation technique and calcinated at 260 °C, showed magnetic ordering at room temperature in an earlier experiment.[12] However, the measured magnetic saturation of 23.6 emu g^{-1} was smaller than undoped magnetite nanoparticles prepared with the coprecipitation technique. Based on our results, the smaller magnetic saturation of this experiment can be partly explained by unintentional hole doping, probably *via* Fe vacancies. In a later experiment on Eu doped magnetite nanoparticles with the morphology of hollow nano-spheres of ~300 nm diameters, the magnetic saturation was found to be higher at 60.81 emu g^{-1} at room temperature upon 3.79% Eu doping.[16] Although this trend quantitatively agrees with our simulation, a direct comparison is impossible since the latter sample was porous. One should note that high surface area and subsequently higher surface spin disorder in magnetite nanoparticles lead to relatively smaller saturation magnetisation than bulk samples. Consequently, the magnetic saturation of magnetite nanoparticles can be as low as ~30 emu g^{-1}.[49] Relatively dense bulk magnetite has a saturation magnetism of ~93 emu g^{-1} at room temperature, equivalent to a

 This journal is © the Owner Societies 2021

Published on 02 September 2021. Downloaded by TU Berlin - Universitaetsbibl on 2/22/2022 10:28:25 AM.

magnetic moment of 3.86 μ_B per f.u. and close to the previously calculated value of $\sim$4.1 μ_B per f.u.[50]

Structurally, all optimised systems deviated from the strict cubic symmetry applied at the beginning of the geometry optimisation process, which was based on pristine Fe_3O_4 above the Verwey transition point. At temperatures above Verwey transition, the pristine cubic Fe_3O_4 unit cell, Fig. 1a, has a lattice parameter of 8.394 Å. Our calculated lattice parameter for pristine ferrimagnetic Fe_3O_4 was 8.431 Å, which agrees well with the measurements. The cubic $Fd\bar{3}m$ geometry has a trigonal primitive representation, which is shown in Fig. 1b. The conventional lattice parameter (a_c) is related to the primitive parameter (a_p) through $a_p = a_c/\sqrt{2}$. For pristine Fe_3O_4, a_p was calculated to be 6.0324 Å. Furthermore, the inclusion of the spin–orbit interaction did not significantly change the calculated lattice parameter relative to collinear calculations (Table S1, ESI†), indicating the negligible structural effect of the spin–orbit interaction in pristine magnetite. Below Verwey transition temperature of $\sim$120 K, however, cubic magnetite undergoes a monoclinic distortion accompanied by a drop in conductivity by two orders of magnitude, which is attributed to the localisation of electrons on two distinct octahedral Fe^{2+} and Fe^{3+} species.[9,10,51,52] Similarly, For Eu_{Fe}, $Eu_{Fe}N_O$, and $Eu_{Fe}F_O$ doped systems, the relaxed primitive parameters, subscripted with p and shown in Table 1, cannot be converted to a conventional cubic system. However, rigorous symmetry detection, with a tolerance of 10^{-4} Å equal to the calculations' accuracy, could relate these primitive cells to less symmetric conventional cells, of which the parameters indicated by subscript c, are also presented in Table 1. Our calculations show that the substitution of Fe by large Eu cations affects the crystal structure and expands the lattice parameters, in line with recent experimental observations in Eu-doped hematite.[53]

Fig. 5 shows the partial DOS of the most stable spin configurations, projected on the x, y, and z axes (frame shown in Fig. 4). One noticeable feature in all three compounds is the empty Eu 4f states, marked with blue circles in Fig. 5a, d, and g, which have a parallel spin direction to the filled states, demonstrating that Eu_{Fe} takes 3+ oxidation state. In Eu^{3+}, only 6 electrons occupy the 4f orbitals while the seventh orbital remains empty. Since in the undoped Fe_3O_4, tetrahedral sites were occupied by Fe^{3+}, one would anticipate that incorporating Eu^{3+} at the tetrahedral site would not change the equal distribution of Fe^{2+} and Fe^{3+} ions in the octahedral sites. However, as we see in the following arguments, this is not the case. As a result, the charge distribution among the Fe ions in the Eu-doped Fe_3O_4 does not conform to the simple designation of spinel or inverse spinel.

In the Fe_3O_4:Eu_{Fe} system, as shown in Fig. 5a, the spin projection on the x axis has the most considerable magnitude, especially for the Fe ions. For Eu, the spin projection on the y and z axes is about one-tenth of the magnitude over the x axis, indicating a slightly larger noncollinearity in the Eu ion, in agreement with the net spin directions of Fig. 4a. Moreover, similar to the case of the undoped Fe_3O_4, all Fe ions are in a high-spin state. However, the remaining tetrahedral Fe has an oxidation state of 2+. For this tetrahedral Fe, the 2+ oxidation state means fully occupied minority spin e and t_2 states and a singly occupied majority spin e orbital (marked with a green arrow in Fig. 5a). Consequently, an octahedral Fe^{2+} should be oxidised to Fe^{3+} to compensate for the tetrahedral Fe^{2+} and maintain charge neutrality. As shown in Table 2, based on net cationic magnetic moments, three out of the four tetrahedral Fe ions are in 3+ oxidation state, having fully occupied majority spin t_{2g} and e_g states and completely empty minority spin t_{2g} and e_g. The fourth octahedral Fe remains in a 2+ oxidation state. For the latter Fe_{Oct} ion, the last electron occupies the minority spin channel of t_{2g} states (marked with a grey arrow in Fig. 5a), separated by $\sim$9 eV from the majority spin states because of the wider crystal field splitting in octahedral coordination—the crystal field for the tetrahedral Fe^{2+} is $\sim$6 eV.

For the hole codoped Fe_3O_4:$Eu_{Fe}N_O$ system, shown in Fig. 5d–f, the hole generated by N doping oxidises an octahedral Fe^{2+} to Fe^{3+}, leaving no Fe^{2+} on octahedral sites. As a result, all octahedral Fe^{3+} ions have fully occupied majority spin t_{2g} and e_g states and empty minority spin t_{2g} and e_g states. Furthermore, for both occupied and empty t_{2g} and e_g states in the x axis projection, some peaks oppose the majority spin states (marked with grey circles in Fig. 5d). These peaks belong to the $Fe_{Oct}(1)$, as marked with a star in Fig. 3, with opposing spin to the rest of Fe_{Oct} ions. The tetrahedral Fe^{2+}, however, is not oxidised by hole doping, as one of its majority-spin e orbitals remains occupied (marked with green arrows in Fig. 5d–f).

For the electron-doped Fe_3O_4:$Eu_{Fe}F_O$ system, unlike the previous two systems, the tetrahedral Fe is in a 3+ oxidation state, just like the undoped Fe_3O_4. The fully occupied spin down e and t_2 states and entirely empty majority spin e and t_2 states verify the 3+ oxidation state of the Fe_{Tet}. Having all the ions that occupy the tetrahedral sites, both Fe_{Tet} and Eu_{Fe}, at 3+ oxidations state implies that at least two of the octahedral Fe ions should be at 2+ oxidation state. Moreover, the electron introduced by F_O doping also must reduce an additional Fe_{Oct}. Consequently, as shown in Table 2, three out of four Fe_{Oct} ions

Table 1 The relaxed primitive lattice parameters (a_p) of the doped systems and their corresponding conventional lattice parameters (a_c), found through a symmetry detecting algorithm. Lattice parameters (a, b, c) are given in Å and angles (α, β, γ) in °. Based on DFT calculations, for pristine Fe_3O_4, $a_p = b_p = c_p = 6.0324$ Å and $\alpha_p = \beta_p = \gamma_p = 60°$

	Fe_3O_4:Eu_{Fe}	Fe_3O_4:$Eu_{Fe}N_O$	Fe_3O_4:$Eu_{Fe}F_O$
a_p	6.214	6.040	6.098
b_p	6.214	6.040	6.098
c_p	6.214	6.201	6.098
α_p	60.00	59.09	60.00
β_p	60.00	59.09	60.00
γ_p	60.00	62.41	60.00
a_c	6.214	10.329	6.098
b_c	6.214	6.259	6.098
c_c	15.221	8.262	14.937
α_c	90.00	90.00	90.00
β_c	90.00	143.10	90.00
γ_c	120.00	90.00	120.00
Group name	$R3m$	$C1m1$	$R3$
Group number	160	8	146

Published on 02 September 2021. Downloaded by TU Berlin - Universitaetsbibl on 2/22/2022 10:28:25 AM.

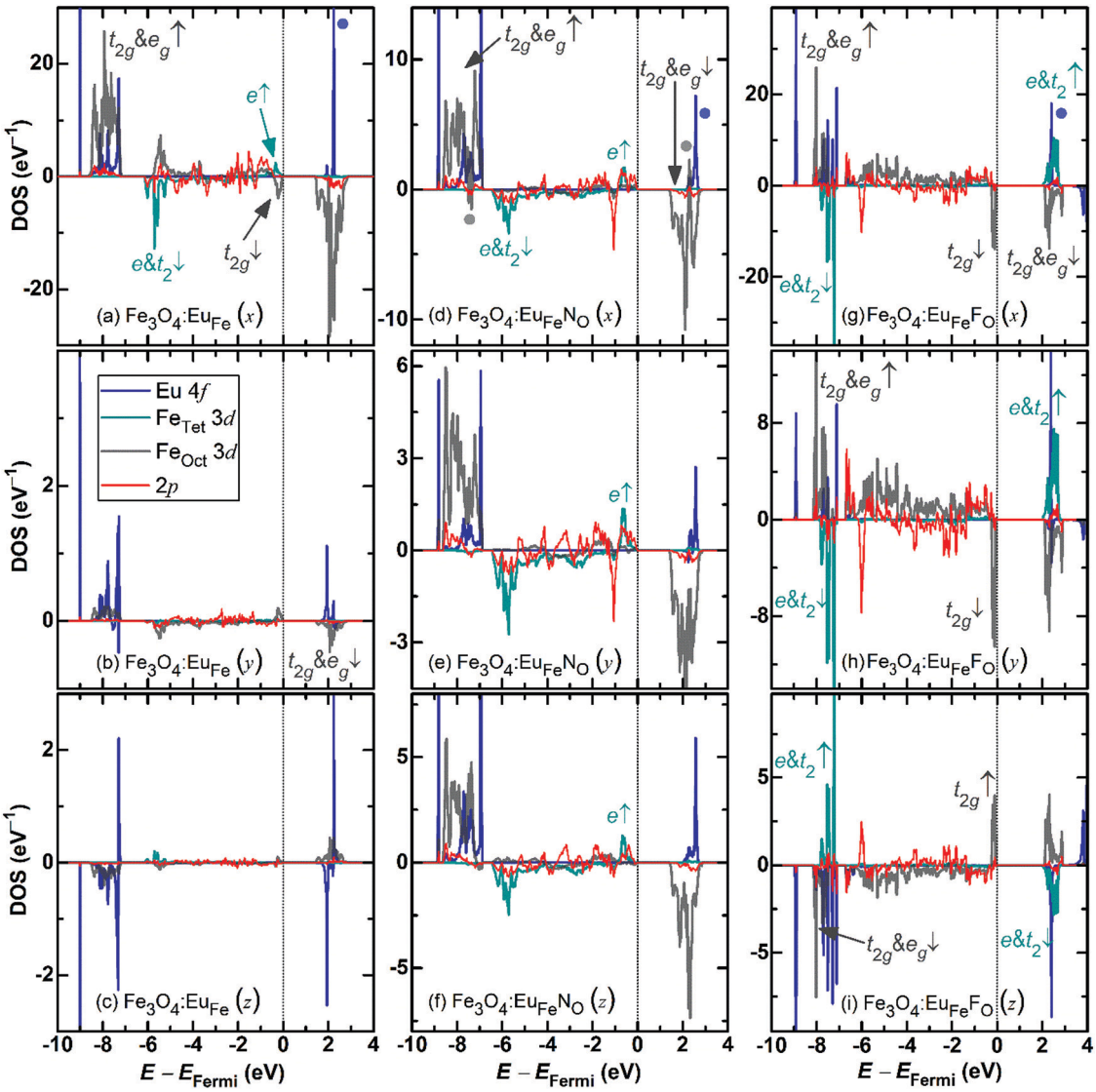

Fig. 5 Partial density of states of the Fe_3O_4:Eu_{Fe} (a–c), Fe_3O_4:$Eu_{Fe}N_O$ (d–f), Fe_3O_4:$Eu_{Fe}F_O$ (g–i), projected on the *x* axis (first row), on *y* axis (second raw) and on *z* axis (third raw). The reference frame used for the projection is showed in Fig. 4.

Table 2 The calculated localised magnetic moment for Eu and all Fe ions. The location of octahedrally coordinated Fe ions is indexed in Fig. 4a. Eu's magnetic moment is smaller than the nominal value because of some degrees of covalency in the Eu–O bond.[47]

System	Fe_3O_4:Eu_{Fe}		Fe_3O_4:$Eu_{Fe}N_O$		Fe_3O_4:$Eu_{Fe}F_O$	
Ion	Magnetic moment (μ_B)	Oxidation state	Magnetic moment (μ_B)	Oxidation state	Magnetic moment (μ_B)	Oxidation state
Eu_{Fe}	4.309	Eu^{3+}	4.354	Eu^{3+}	4.447	Eu^{3+}
Fe_{Tet}	3.699	Fe^{2+}	3.722	Fe^{2+}	4.169	Fe^{3+}
$Fe_{Oct}(1)$	3.805	Fe^{2+}	4.275	Fe^{3+}	3.744	Fe^{2+}
$Fe_{Oct}(2)$	4.334	Fe^{3+}	4.246	Fe^{3+}	3.744	Fe^{2+}
$Fe_{Oct}(3)$	4.335	Fe^{3+}	4.327	Fe^{3+}	4.325	Fe^{3+}
$Fe_{Oct}(4)$	4.337	Fe^{3+}	4.277	Fe^{3+}	3.744	Fe^{2+}

in the supercell are in a 2+ oxidation state. The additional electron in all Fe^{2+} ions occupies the minority spin t_{2g} states as marked in grey arrows in Fig. 5g–i.

The DOS of the Fe_3O_4:Eu_{Fe}, Fe_3O_4:$Eu_{Fe}N_O$ and Fe_3O_4:$Eu_{Fe}F_O$ systems show a bandgap of ~1 eV, which is wider than the 0.14 eV experimentally reported for pristine Fe_3O_4,[54] below Verwey transition at 115 K.[52,55] This bandgap can be explained based on the empirical clues that accompany the bandgap below Verwey transition. These clues are the lowered crystal symmetry from cubic to uniaxial symmetry and the ordering of

 This journal is © the Owner Societies 2021

Published on 02 September 2021. Downloaded by TU Berlin - Universitaetsbibl on 2/22/2022 10:28:25 AM.

the Fe^{3+} and Fe^{2+} ions on the octahedral sites, observed in magnetite below Verwey temperature, that promote the broadening of the bandgap. As seen in Table 2, Eu doping alone or with carrier codoping lowers the crystal symmetry. Moreover, as shown in Table 1, an obvious degree of charge disproportionation can be seen among Fe ions in the Eu-doped and carrier codoped Fe_3O_4 systems. Corroborating our results, many earlier DFT calculations that predicted semimetallic conduction for Fe_3O_4 were based on either LDA[56] or GGA[57] level of the theory. These calculations also often reported a uniform oxidation state for Fe_{Oct} of $\sim$+2.5 without acknowledging the charge disproportionation. This inconsistency is due to the inaccurate description of the exchange term, which typically results in the delocalisation of electrons over the system for standard DFT functionals. However, DFT calculations performed with higher-level theory such as DFT+U[58] or Hartree–Fock hybrid DFT[59] can effectively localise d and f electrons in strongly correlated systems, which predicts a charge disproportionation among Fe_{Oct}, showing also a bandgap. However, the width of this bandgap is very sensitive to the functional parameters used, but not the charge disproportionation itself. Some also further hypothesised the existence of a bandgap within the bulk of Fe_3O_4 even above the Verwey transition temperature, attributing the observed conductivity to small polaron hopping instead of band semimetallicity.[60]

Lanthanide doped magnetite has widely been used as a base or substrate for magnetically recoverable catalysts.[12,26,61] Nonetheless, successful recovery requires a strong magnetic response to facilitate magnetic decantation with a permanent magnet.[13,62] The magnetic attraction between magnetite particles and the permanent magnet is a dipole–dipole interaction proportional to the magnetite's saturation magnetisation.[63] In undoped Fe_3O_4, the large magnetisation of $\sim$4.1 μ_B and amply high Curie temperature guarantee ease of magnetic separation at ambient conditions.[8] Given that Fe_3O_4:Eu_{Fe} has a magnetisation that is about twice as large as Fe_3O_4's, Eu doping is predicted here to enhance the efficiency of magnetic decantation of catalyst particles. The same statement is also true for the electron codoped system, Fe_3O_4:$Eu_{Fe}F_O$, in which the ground state magnetic phase is not as stable, but competing magnetic phases still produce large magnetisation. However, for hole codoped Fe_3O_4:$Eu_{Fe}N_O$, given the instability of the ground phase and the small magnetisation of the competing phase, one anticipates a drop in the efficiency of magnetic decantation. As a result, one must make sure that in preparing Eu-doped Fe_3O_4, no unintentional hole doping occurs. Magnetite tends to be Fe deficient on octahedral sites.[64] These Fe vacancies can be the source of p-type doping in magnetite, which are to be avoided for utilising the full magnetic effect of Eu doping. Lastly, since the noncollinearity is caused by Eu's larger mass, the spin–orbit interaction in Fe compounds containing heavier elements[65–67] would be expected to play a major role, similar to Fe_3O_4:Eu_{Fe}, and therefore, is quite interesting to investigate.

Conclusions

We examined the spin alignments among the Fe and Eu ions in Eu-doped magnetite using noncollinear density functional theory at the DFT+U level. We simulated additional carrier codoping by replacing N for O for producing holes and replacing F for O for producing electrons. We found that Eu dopant preferably substitutes tetrahedral Fe in magnetite, either with or without carrier codoping. In all cases, Eu_{Fe} was stabilised in a 3+ oxidation state, and its spin was at a near-complete angle to the remaining Fe_{Tet}, resulting in smaller spin cancellations when compared to the undoped magnetite. This situation results in more substantial saturation magnetisation. The net magnetic moment for Fe_3O_4:Eu_{Te}, Fe_3O_4:$Eu_{Te}N_O$, and Fe_3O_4:$Eu_{Te}F_O$, was 9.451 μ_B per f.u., 4.929 μ_B per f.u., and 7.937 μ_B per f.u., respectively. Finally, hole codoping was found to destabilise the magnetic ground state, lowering the saturation magnetisation and ordering temperature. Electron codoping, however, was not predicted to significantly decrease the saturation magnetisation.

Conflicts of interest

There are no conflicts to declare.

Acknowledgements

The authors gratefully acknowledge the funding of this project by computing time provided by the Paderborn Center for Parallel Computing (PC^2). JJGM acknowledges the support from the FusionCAT project (001-P-001722) co-financed by the European Union Regional Development Fund within the framework of the ERDF Operational Program of Catalonia 2014-2020 with a grant of 50% of total cost eligible.

References

1 A. Muxworthy and E. McClelland, Review of the low-temperature magnetic properties of magnetite from a rock magnetic perspective, *Geophys. J. Int.*, 2000, **140**, 101–114.
2 C. Su, Environmental implications and applications of engineered nanoscale magnetite and its hybrid nanocomposites: a review of recent literature, *J. Hazard. Mater.*, 2017, **322**, 48–84.
3 M. Opel, Spintronic oxides grown by laser-MBE, *J. Phys. D: Appl. Phys.*, 2011, **45**, 033001.
4 G. S. Parkinson, U. Diebold, J. Tang and L. Malkinski, in *Advanced Magnetic Materials*, ed. L. Malkinski, IntechOpen, 2012, pp. 61–89.
5 M. B. Gawande, P. S. Branco and R. S. Varma, Nano-magnetite (Fe_3O_4) as a support for recyclable catalysts in the development of sustainable methodologies, *Chem. Soc. Rev.*, 2013, **42**, 3371–3393.
6 R. A. Revia and M. Zhang, Magnetite nanoparticles for cancer diagnosis, treatment, and treatment monitoring: recent advances, *Mater. Today*, 2016, **19**, 157–168.
7 J. Mürbe, A. Rechtenbach and J. Töpfer, Synthesis and physical characterization of magnetite nanoparticles for biomedical applications, *Mater. Chem. Phys.*, 2008, **110**, 426–433.

Published on 02 September 2021. Downloaded by TU Berlin - Universitaetsbibl on 2/22/2022 10:28:25 AM.

8 S. K. Banerjee and B. M. Moskowitz, in *Magnetite biomineralization and magnetoreception in organisms*, ed. J. L. Kirschvink, D. S. Jones and B. J. MacFadden, Springer, Boston, MA, 1985, ch. 2, pp. 17–41.
9 J. P. Wright, J. P. Attfield and P. G. Radaelli, Charge ordered structure of magnetite Fe_3O_4 below the Verwey transition, *Phys. Rev. B: Condens. Matter Mater. Phys.*, 2002, **66**, 214422.
10 S. Klotz, G. Rousse, T. Strässle, C. L. Bull and M. Guthrie, Nuclear and magnetic structure of magnetite under pressure to 5.3 GPa and at low temperatures to 130 K by neutron scattering, *Phys. Rev. B: Condens. Matter Mater. Phys.*, 2006, **74**, 012410.
11 J. Ma, Y. Wang, J. Niu and X. Shen, Synthesis and Characterization of La-Doped Fe3O4-Polyaniline Magnetic Response Nanocomposites, *J. Macromol. Sci., Part B: Phys.*, 2006, **45**, 533–540.
12 C. R. De Silva, S. Smith, I. Shim, J. Pyun, T. Gutu, J. Jiao and Z. Zheng, Lanthanide(III)-doped magnetite nanoparticles, *J. Am. Chem. Soc.*, 2009, **131**, 6336–6337.
13 F. Zhang and D. Zhao, Fabrication of ordered magnetite-doped rare earth fluoride nanotube arrays by nanocrystal self-assembly, *Nano Res.*, 2009, **2**, 292–305.
14 C. Mi, J. Zhang, H. Gao, X. Wu, M. Wang, Y. Wu, Y. Di, Z. Xu, C. Mao and S. Xu, Multifunctional nanocomposites of superparamagnetic (Fe_3O_4) and NIR-responsive rare earth-doped up-conversion fluorescent (NaYF4: Yb, Er) nanoparticles and their applications in biolabeling and fluorescent imaging of cancer cells, *Nanoscale*, 2010, **2**, 1141–1148.
15 D. Padalia, U. Johri and M. Zaidi, Study of cerium doped magnetite (Fe_3O_4:Ce)/PMMA nanocomposites, *Phys. B*, 2012, **407**, 838–843.
16 W. Huan, C. Cheng, Y. Yang, H. Yuan and Y. Li, A Study on the Magnetic and Photoluminescence Properties of Eu^{n+} and Sm^{3+} Doped Fe3O4 Nanoparticles, *J. Nanosci. Nanotechnol.*, 2012, **12**, 4621–4634.
17 K. P. Rice, S. E. Russek, R. H. Geiss, J. M. Shaw, R. J. Usselman, E. R. Evarts, T. J. Silva, H. T. Nembach, E. Arenholz and Y. U. Idzerda, Temperature-dependent structure of Tb-doped magnetite nanoparticles, *Appl. Phys. Lett.*, 2015, **106**, 062409.
18 W. Huan, G. Ji, C. Cheng, J. An, Y. Yang and X. Liu, Preparation, characterization of high-luminescent and magnetic Eu^{3+}, Dy^{3+} doped superparamagnetic nano-Fe_3O_4, *J. Nanosci. Nanotechnol.*, 2015, **15**, 1780–1788.
19 G. Gao, Q. Zhang, X.-B. Cheng, R. Sun, J. G. Shapter, T. Yin and D. Cui, Synthesis of three-dimensional rare-earth ions doped CNTs-GO-Fe3O4 hybrid structures using one-pot hydrothermal method, *J. Alloys Compd.*, 2015, **649**, 82–88.
20 O. Polozhentsev, S. Kubrin, V. Butova, V. Kochkina, A. Soldatov and V. Stashenko, Structure and magnetic properties of pure and samarium doped magnetite nanoparticles, *J. Struct. Chem.*, 2016, **57**, 1459–1468.
21 H. Zhang, V. Malik, S. Mallapragada and M. Akinc, Synthesis and characterization of Gd-doped magnetite nanoparticles, *J. Magn. Magn. Mater.*, 2017, **423**, 386–394.
22 A. Petran, T. Radu, G. Borodi, A. Nan, M. Suciu and R. Turcu, Effects of rare earth doping on multi-core iron oxide nanoparticles properties, *Appl. Surf. Sci.*, 2018, **428**, 492–499.
23 R. Jain, V. Luthra and S. Gokhale, Probing influence of rare earth ions (Er^{3+}, Dy^{3+} and Gd^{3+}) on structural, magnetic and optical properties of magnetite nanoparticles, *J. Magn. Magn. Mater.*, 2018, **456**, 179–185.
24 P. Alimard, Fabrication and kinetic study of Nd-Ce doped Fe3O4-chitosan nanocomposite as catalyst in Fenton dye degradation, *Polyhedron*, 2019, **171**, 98–107.
25 R. Jain, V. Luthra, M. Arora and S. Gokhale, Infrared spectroscopic study of magnetic behavior of dysprosium doped magnetite nanoparticles, *J. Supercond. Novel Magn.*, 2019, **32**, 325–333.
26 Y. Orooji, M. H. Irani-Nezhad, R. Hassandoost, A. Khataee, S. R. Pouran and S. W. Joo, Cerium doped magnetite nanoparticles for highly sensitive detection of metronidazole via chemiluminescence assay, *Spectrochim. Acta, Part A*, 2020, **234**, 118272.
27 R. Kershi, F. Ali and M. Sayed, Influence of rare earth ion substitutions on the structural, optical, transport, dielectric, and magnetic properties of superparamagnetic iron oxide nanoparticles, *J. Adv. Ceram.*, 2018, **7**, 218–228.
28 T. Lastovina, A. Budnyk, E. Kudryavtsev, A. Nikolsky, A. Kozakov, N. Chumakov, A. Emelyanov and A. Soldatov, Solvothermal synthesis of Sm^{3+}-doped Fe_3O_4 nanoparticles, *Mater. Sci. Eng. C*, 2017, **80**, 110–116.
29 G. Spavieri and M. Mansuripur, Origin of the spin–orbit interaction, *Phys. Scr.*, 2015, **90**, 085501.
30 D. Bercioux and P. Lucignano, Quantum transport in Rashba spin-orbit materials: a review, *Rep. Prog. Phys.*, 2015, **78**, 106001.
31 K. Shanavas, Z. S. Popović and S. Satpathy, Theoretical model for Rashba spin-orbit interaction in d electrons, *Phys. Rev. B: Condens. Matter Mater. Phys.*, 2014, **90**, 165108.
32 P. Weinberger, *Current Problems in Condensed Matter*, Springer, 1998, ch. 87, pp. 87–93.
33 G. Kresse and J. Hafner, *Ab initio* molecular dynamics for liquid metals, *Phys. Rev. B: Condens. Matter Mater. Phys.*, 1993, **47**, 558–561.
34 G. Kresse and J. Hafner, *Ab initio* molecular-dynamics simulation of the liquid-metal–amorphous-semiconductor transition in germanium, *Phys. Rev. B: Condens. Matter Mater. Phys.*, 1994, **49**, 14251–14269.
35 G. Kresse and D. Joubert, From ultrasoft pseudopotentials to the projector augmented-wave method, *Phys. Rev. B: Condens. Matter Mater. Phys.*, 1999, **59**, 1758–1775.
36 J. P. Perdew, K. Burke and M. Ernzerhof, Generalized Gradient Approximation Made Simple, *Phys. Rev. Lett.*, 1996, **77**, 3865–3868.
37 A. I. Liechtenstein, V. I. Anisimov and J. Zaanen, Density-functional theory and strong interactions: Orbital ordering in Mott-Hubbard insulators, *Phys. Rev. B: Condens. Matter Mater. Phys.*, 1995, **52**, R5467–R5470.
38 P. Larson, W. R. Lambrecht, A. Chantis and M. van Schilfgaarde, Electronic structure of rare-earth nitrides using the LSDA+U approach: importance of allowing 4 f orbitals to

 This journal is © the Owner Societies 2021

Published on 02 September 2021. Downloaded by TU Berlin - Universitaetsbibl on 2/22/2022 10:28:25 AM.

break the cubic crystal symmetry, *Phys. Rev. B: Condens. Matter Mater. Phys.*, 2007, **75**, 045114.

39 S. Sanna, W. Schmidt, T. Frauenheim and U. Gerstmann, Rare-earth defect pairs in GaN:LDA+U calculations, *Phys. Rev. B: Condens. Matter Mater. Phys.*, 2009, **80**, 104120.

40 N. Deilynazar, E. Khorasani, M. Alaei and S. J. Hashemifar, First-principles insights into f magnetism: A case study on some magnetic pyrochlores, *J. Magn. Magn. Mater.*, 2015, **393**, 127–131.

41 T. Kendelewicz, S. Kaya, J. T. Newberg, H. Bluhm, N. Mulakaluri, W. Moritz, M. Scheffler, A. Nilsson, R. Pentcheva and G. E. Brown, X-ray Photoemission and Density Functional Theory Study of the Interaction of Water Vapor with the Fe_3O_4(001) Surface at Near-Ambient Conditions, *J. Phys. Chem. C*, 2013, **117**, 2719–2733.

42 D. Odkhuu, P. Taivansaikhan, W. S. Yun and S. C. Hong, A first-principles study of magnetostrictions of Fe_3O_4 and $CoFe_2O_4$, *J. Appl. Phys.*, 2014, **115**, 17A916.

43 M. H. N. Assadi and D. A. H. Hanaor, The effects of copper doping on photocatalytic activity at (101) planes of anatase TiO_2: A theoretical study, *Appl. Surf. Sci.*, 2016, **387**, 682–689.

44 K. Sato and H. Katayama-Yoshida, First principles materials design for semiconductor spintronics, *Semicond. Sci. Technol.*, 2002, **17**, 367–376.

45 A. Boonchun, N. Umezawa, T. Ohno, S. Ouyang and J. Ye, Role of photoexcited electrons in hydrogen evolution from platinum co-catalysts loaded on anatase TiO2: a first-principles study, *J. Mater. Chem. A*, 2013, **1**, 6664–6669.

46 A. Pham, M. H. N. Assadi, A. B. Yu and S. Li, Critical role of Fock exchange in characterizing dopant geometry and magnetic interaction in magnetic semiconductors, *Phys. Rev. B: Condens. Matter Mater. Phys.*, 2014, **89**, 155110.

47 M. H. N. Assadi and H. Katayama-Yoshida, Covalency a Pathway for Achieving High Magnetisation in $TMFe_2O_4$ Compounds, *J. Phys. Soc. Jpn.*, 2019, **88**, 044706.

48 G. Samara and A. Giardini, Effect of pressure on the Néel temperature of magnetite, *Phys. Rev.*, 1969, **186**, 577–580.

49 G. F. Goya, T. S. Berquó, F. C. Fonseca and M. P. Morales, Static and dynamic magnetic properties of spherical magnetite nanoparticles, *J. Appl. Phys.*, 2003, **94**, 3520–3528.

50 D. J. Huang, C. F. Chang, H. T. Jeng, G. Y. Guo, H. J. Lin, W. B. Wu, H. C. Ku, A. Fujimori, Y. Takahashi and C. T. Chen, Spin and Orbital Magnetic Moments of Fe_3O_4, *Phys. Rev. Lett.*, 2004, **93**, 077204.

51 E. Verwey, Electronic conduction of magnetite (Fe_3O_4) and its transition point at low temperatures, *Nature*, 1939, **144**, 327–328.

52 F. Walz, The Verwey transition-a topical review, *J. Phys.: Condens. Matter*, 2002, **14**, R285–R340.

53 C. Stanhaus, L. L. S. Alves, J. L. Ferrari, J. C. Padilha and M. S. Góes, Hematite (α-Fe_2O_3) pure and doped with Eu^{3+} obtained by high-energy ball milling process, *Mater. Chem. Phys.*, 2020, **254**, 123385.

54 A. Chainani, T. Yokoya, T. Morimoto, T. Takahashi and S. Todo, High-resolution photoemission spectroscopy of the Verwey transition in Fe_3O_4, *Phys. Rev. B: Condens. Matter Mater. Phys.*, 1995, **51**, 17976–17979.

55 E. Verwey and P. Haayman, Electronic conductivity and transition point of magnetite (Fe_3O_4), *Physica*, 1941, **8**, 979–987.

56 Z. Zhang and S. Satpathy, Electron states, magnetism, and the Verwey transition in magnetite, *Phys. Rev. B: Condens. Matter Mater. Phys.*, 1991, **44**, 13319–13331.

57 S. Ju, T.-Y. Cai, H.-S. Lu and C.-D. Gong, Pressure-Induced Crystal Structure and Spin-State Transitions in Magnetite (Fe_3O_4), *J. Am. Chem. Soc.*, 2012, **134**, 13780–13786.

58 M. H. N. Assadi, J. J. Gutiérrez Moreno and M. Fronzi, High-Performance Thermoelectric Oxides Based on Spinel Structure, *ACS Appl. Energy Mater.*, 2020, **3**, 5666–5674.

59 A. D. Rowan, C. H. Patterson and L. V. Gasparov, Hybrid density functional theory applied to magnetite: Crystal structure, charge order, and phonons, *Phys. Rev. B: Condens. Matter Mater. Phys.*, 2009, **79**, 205103.

60 H. Liu and C. Di Valentin, Band gap in magnetite above Verwey temperature induced by symmetry breaking, *J. Phys. Chem. C*, 2017, **121**, 25736–25742.

61 V. Polshettiwar, R. Luque, A. Fihri, H. Zhu, M. Bouhrara and J.-M. Basset, Magnetically Recoverable Nanocatalysts, *Chem. Rev.*, 2011, **111**, 3036–3075.

62 P. Riente, C. Mendoza and M. A. Pericás, Functionalization of Fe_3O_4 magnetic nanoparticles for organocatalytic Michael reactions, *J. Mater. Chem.*, 2011, **21**, 7350–7355.

63 Y. Zhu, L. P. Stubbs, F. Ho, R. Liu, C. P. Ship, J. A. Maguire and N. S. Hosmane, Magnetic nanocomposites: a new perspective in catalysis, *ChemCatChem*, 2010, **2**, 365–374.

64 L. Blaney, Magnetite (Fe_3O_4): properties, synthesis, and applications, *Lehigh Rev.*, 2007, **15**, 33–81.

65 G. Gökoğlu and E. Aktürk, Half metallicity and pressure-induced electronic structure of monolayer FeX2 (X = S, Se), *Mater. Res. Express*, 2017, **4**, 116305.

66 R. Mahat, S. Kc, D. Wines, F. Ersan, S. Regmi, U. Karki, R. White, C. Ataca, P. Padhan, A. Gupta and P. LeClair, Tuneable structure and magnetic properties in $Fe_{3-x}V_xGe$ alloys, *J. Alloys Compd.*, 2020, **830**, 154403.

67 R. Mahat, S. Kc, D. Wines, S. Regmi, U. Karki, Z. Li, F. Ersan, J. Law, C. Ataca, V. Franco, A. Gupta and P. LeClair, Influence of Cr-substitution on the structural, magnetic, electron transport, and mechanical properties of $Fe_{3-x}Cr_xGe$ Heusler alloys, *J. Magn. Magn. Mater.*, 2021, **521**, 167398.